

# Electron Channeling Contrast Imaging for the Characterization of Dislocations in III—V Thin Films on Silicon (001)

Laura Monge-Bartolome,\* Paula Mouriño Miñambres, Alicia Peiro Codoñer, Miguel Sinusia Lozano, Zhao Yan, Ivan Garcia Vara, Thierry Baron, Qiang Li, and Víctor J. Gómez

Characterization of defects is essential for the semiconductor industry, as they can be detrimental to device performance. Electron channeling contrast imaging (ECCI) is an electron diffraction technique performed in a scanning electron microscope that has emerged as a fast and nondestructive technique for defect characterization. Herein, ECCI is applied to the characterization of extended defects in the heteroepitaxy of III-V semiconductor thin films on silicon. The influence of the electron-beam parameters (beam energy and current) is studied to optimize the ECCI micrographs. Additionally, the influence of the diffraction condition on the visibility and contrast of two types of extended defectsthreading dislocations and stacking faults—is studied. Moreover, the influence of the diffraction conditions on the density of extended defects measured in the ECCI micrographs is studied, giving a lower limit of the extended defects density. This work shows that ECCI is a promising technique for deep study of extended defects in the heteroepitaxy of III-V semiconductor thin films on Si, revealing a huge potential for wafer mapping, which is crucial for homogeneity testing and scalability.

1. Introduction

Fast, low-cost, and nondestructive characterization of extended defects is critical for the optimization of the heteroepitaxy of III–V semiconductors on silicon. Specially now when the limits of electronics are being reached, silicon photonics has emerged as one of the most promising technologies to overcome these

limitations thanks to the numerous advantages that this technology provides, such as well-developed industry, large scalability, cost-effective as well as desired optical and electrical properties.<sup>[1]</sup> However, silicon is not suitable for the realization of certain type of active devices, for example, optical modulators due to the lack of strong electro-optic effect, or lasers due to its indirect bandgap nature. III-V materials are the best candidates to overcome these limitations. Monolithic integration (direct growth) of III-V materials on Si, even being in research state, is the most promising approach regarding scalability and reductions of cost and material waste. [2-4] However, the direct growth of III-V materials on Si brings new challenges, one of those is caused by the lattice mismatch between silicon and III-V materials. Lattice mismatch generates defects such as dislocations that go through the active materials degrading device

performance.<sup>[5]</sup> Fast, cost-effective, and nondestructive characterization techniques are essential for the development of monolithic integration of III–Vs on silicon.

The most widely used technique for structural defect characterization is transmission electron microscopy (TEM). Thanks to its very high resolution, it allows the observation of defects down to the atomic level. However, TEM needs the fabrication of lamella

L. Monge-Bartolome, P. Mouriño Miñambres, A. Peiro Codoñer, M. Sinusia Lozano, V. J. Gómez Nanophotonics Technology center Universitat Politècnica de València CP 46022 Valencia, Spain E-mail: Imonge@ntc.upv.es

The ORCID identification number(s) for the author(s) of this article can be found under https://doi.org/10.1002/pssa.202500580.

© 2025 The Author(s). physica status solidi (a) applications and materials science published by Wiley-VCH GmbH. This is an open access article under the terms of the Creative Commons Attribution-NonCommercial-NoDerivs License, which permits use and distribution in any medium, provided the original work is properly cited, the use is non-commercial and no modifications or adaptations are made.

DOI: 10.1002/pssa.202500580

Z. Yan, Q. Li School of Physics and Astronomy Cardiff University Cardiff CF24 3AA, UK

I. Garcia Vara Instituto de Energía Solar Universidad Politécnica de Madrid CP 28040 Madrid, Spain

T. Baron CNRS, CEA-LETI, LTM Univ. Grenoble Alpes CP 38054 Grenoble, France for sample observation, this makes this technique destructive as well as time consuming and expensive. Additionally, the observation area is restricted to the lamella size, typically a few µm<sup>2</sup>.<sup>[6]</sup> Within this context, electron channeling contrast imaging (ECCI) using a scanning electron microscope (SEM) has emerged as a fast and nondestructive technique for defect characterization. It is based on the analysis of the contrast of backscattered electrons (BSE). [7] In addition, it allows the characterization of large areas of materials, that is, wafer mapping. [8] To be capable to perform ECCI measurements it is necessary to satisfy channeling conditions: the relative orientation of the electron beam to the crystalline lattice need to fulfill the Bragg condition. It is achieved at the band edge of Kikuchi bands, where the BSE intensity is minimal.<sup>[9]</sup> When the Bragg condition is fulfilled, any distortion of the crystal lattice, such as dislocations, generates a change in contrast of the BSE. [10] In addition to providing fast feedback, ECCI also allows a deep study of defects, such as preferential types of dislocations, planes, or directions, as well as the study of individual dislocations (Burgers vector **b** analysis).<sup>[10]</sup> Therefore, ECCI is a versatile tool with high potential for the characterization of extended defects in semiconductors.[8,11-13]

Despite ECCI in an SEM has been successfully employed for the characterization of dislocations in a plethora of systems such as GaAs-on-Si virtual substrates, [14,15] GaAs-on-GaPon-Si, $^{[16]}$  InGaAs-on-InP, $^{[17]}$  GaP-on-Si, $^{[8,11,18]}$  GaSb-on-Si, $^{[19]}$ GaN-on-SiC, [20] and III-V nanostructures [21,22]—none of them show a comprehensive analysis of how to apply ECCI to the characterization of extended defects in the heteroepitaxial growth of III-V semiconductors. In this work, we present a comprehensive analysis of the measurement conditions to perform ECCI on III-V thin films using a retractable versatile backscattered electron detector (VBED). Two different III-V thin films grown on silicon have been used for this work. First, Ga(In)As thin films with a Ge buffer layer on Si, and GaSb thin films grown on commercial GaSb-on-Si(100) templates. Both sets of samples were grown by metal organic vapor phase epitaxy (MOVPE). Samples with a high density of defects have been chosen for this study. First, we study the influence of the beam energy and current on the contrast between topography and defects and on the signal-tonoise ratio (SNR), respectively. After optimizing beam energy and current, we performed an exhaustive analysis of the differences between ECCI micrographs taken at different diffraction conditions. We show that diffraction conditions are critical for the visualization of extended defects. For example, defects can appear as points for specific diffraction conditions, whereas for others they can appear as lines. This study will thereby aim at increasing the knowledge on the characterization of the heteroepitaxy of III–V semiconductors on silicon.

# 2. Methodology

# 2.1. Equipment

ECCI measurements were performed in a field emission SEM (FE-SEM Jeol IT800 SHL) operated at beam energies ranging from 10 to 30 kV and beam currents from 0.2 to 5.7 nA with an angular multisegment retractable detector in backscatter configuration, known as VBED (**Figure 1**a), and an Everhart—Thornley secondary electron (SE) detector. Electron channeling pattern (ECP) is observed by the SE detector (Everhart—Thornley) when lower scan coils and lower shift coils are disabled; therefore, the beam is rocking on the sample instead of scanning.

## 2.2. Samples

The samples under study are: i) Ga(In)As thin film grown on heavily dislocated Ge-on-Si(100) templates. First, a Ge thin film of 120 nm was deposited in a standard 13.56 MHz capacitively coupled with radio frequency plasma-enhanced chemical vapor deposition equipment on Si (100) with 5° miscut toward <111>. Then, a 330 nm thick Ga(In)As capping layer was grown by MOVPE, in a horizontal, low-pressure AIX200/4 reactor, using arsine (AsH<sub>3</sub>), phosphine (PH<sub>3</sub>), trimethyl gallium (TMGa), trimethyl indium (TMIn), trimethyl aluminum (TMAl), dimethyl

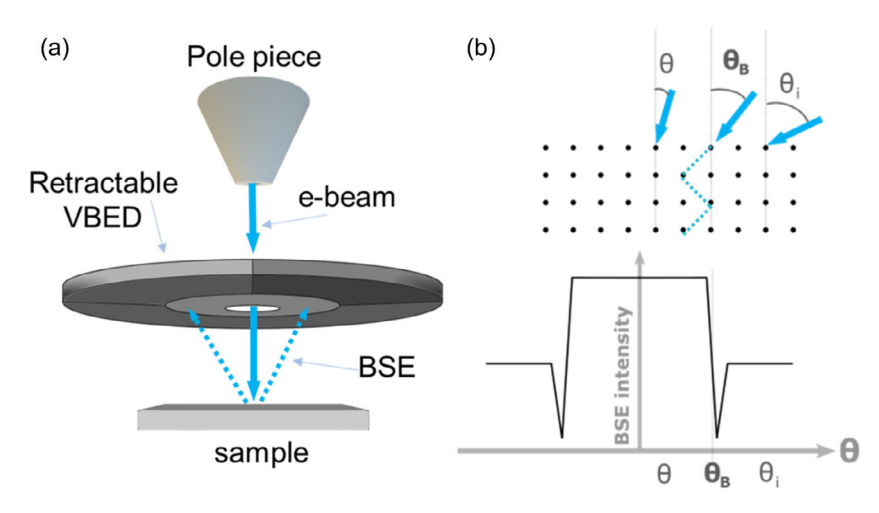


Figure 1. a) Schematic illustration (not to scale) of the pole piece, retractable VBED detector and sample. The detector is composed by a central inner circular segment together with an external outer segment divided into four quadrants. b) Schematic of the BSE intensity as a function of the angle between the zone axis of the crystal and the incident electron beam.

zinc (DMZn), di-tert-butylsilane (DTBSi), and diethyl tellurium (DETe) as precursor molecules.  $\,$ 

ii) GaSb-based thin film grown on Si. 250 nm GaSb thick films were grown by MOVPE on commercial 1 µm thick GaSb-on-Si(100) templates (manufactured by Floralis) in an Aixtron close-coupled showerhead system. The precursors used were TEGa, triethyl antimony (TESb), TMIn, and tertiary-butyl arsine (TBAs). Prior to the growth, the sample must go under a thermal treatment for oxide desorption at 590 °C for 5 min. Then, a 120 nm thick GaSb layer is grown. Next, a InGaSb/GaSb (12/10 nm) strained layer superlattice of 10 periods, and finally a 300 nm thick capping GaSb layer.

## 2.3. ECCI Working Principle

ECCI is an electron diffraction technique, the studied signal is BSE that elastically interact with the atoms of the crystal lattice. The intensity of the BSE depends on the angle between the zone axis of the crystal and the incident electron beam<sup>[7]</sup> as shown in Figure 1b.

Starting when the incident beam is parallel to the zone axis or with a small angle, the BSE signal is strong. The signal remains high until the Bragg condition is fulfilled ( $n\lambda = 2d \sin\theta_B$ ). Being n an integer,  $\lambda$  the wavelength of the incident electron beam, d the distance between the crystal planes. The BSE signal suffers a sudden drop because the scattering angle drives electrons along the crystal. This phenomenon is called channeling. For greater angles, the BSE signal increases, but the yield is lower than for angles smaller than the  $\theta_B$ . This profile is also known as Kikuchi band. [23] Regarding the abrupt change of the BSE yield at the Bragg angle or edge of the Kikuchi band, any distortions of the crystal lattice, that is, dislocations, will produce high contrast on the BSE signal. Therefore, ECCI measurements are performed with the sample aligned to the Bragg condition.

Prior to perform ECCI, and to be able to properly align the sample with the electron beam, it is necessary to measure the ECP.<sup>[24]</sup> The ECP is performed by rocking the electron beam over the sample, thus the Kikuchi bands are visible when the Bragg condition is fulfilled for each particular set of crystalline lattice planes. A ECP of GaSb crystal is shown in **Figure 2**. By rotating and tilting the sample, the beam is positioned on the edge of the desired Kikuchi band to perform the measurements. ECP in combination with the software JCrystalSoft<sup>[25]</sup> allows indexing the Kikuchi bands and therefore to perform ECCI at a known diffraction condition.

In general, ECCI is a surface-sensitive characterization technique, where the BSE that contribute to the ECCI signal come from a depth range between 10 and 100 nm. The main limiting factor to the depth resolution is the loss of electrons due to scattering events, that produces a broadening and damping of the impinging electron wave front (channeled electrons), as a function of depth into the crystal. Nonetheless, some degree of depth resolution has been demonstrated in previous works on GaP/Si, SiGe/Si, and InGaAs/GaAs heterostructures, [18,26,27] where misfit dislocations buried at the heteroepitaxial interface were imaged using ECCI at depths of up to 100 nm.

The samples selected for this study are Ga(In)As and GaSb grown on Si(001). Both Ga(In)As and GaSb have a face-centered

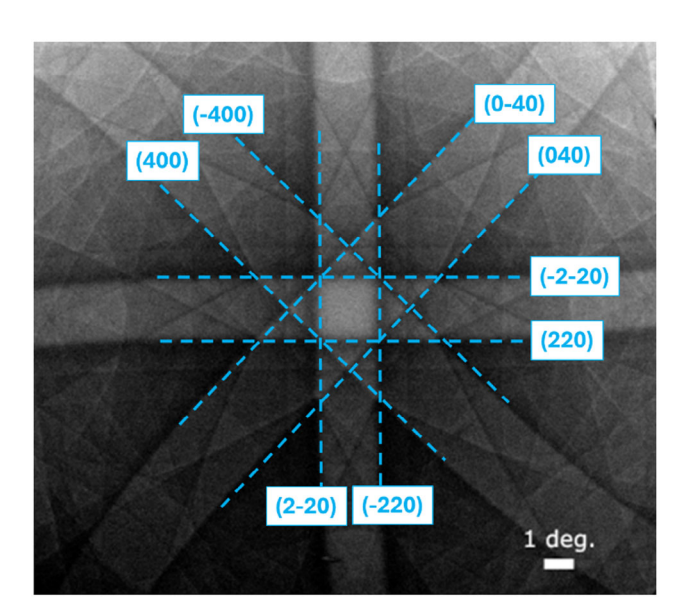


Figure 2. ECP of the 1 µm GaSb-on-Si template.

cubic crystalline structure. Being (001) the zone axis, the families of planes that have stronger contrast are {220} and {400}.

# 3. Experimental Results

#### 3.1. Beam Parameters

Regarding electron-beam parameters, the study of the effects of beam energy and current was performed on the Ga(In)As on Si samples.

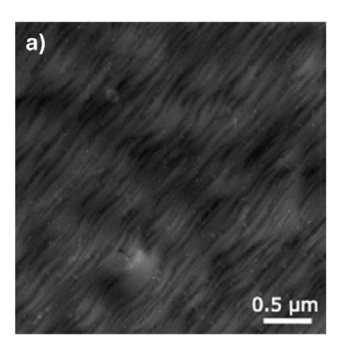
**Figure 3**a shows a SE micrograph of the sample, where the topography is observed. Figure 3b,c shows ECCI micrographs of the same sample at the same area with beam energies of 10 and 30 kV respectively. First, to align the electron beam with the crystal lattice, ECP images were recorded (inset of Figure 3b,c). It is worth noting that the width of the Kikuchi bands decreases when increasing the beam energy. This can be attributed to the decrease of the wavelength of the electrons when the beam energy is increased. Therefore, following the Bragg law  $(n\lambda = 2d \sin\theta_B)$ , for the same distance between the lattice planes,  $\theta_B$  is smaller.

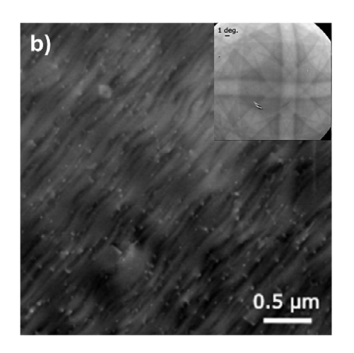
It can be observed that in the measurement performed at 10 kV, the contribution of the topography was higher than for 30 kV, while in the image at 30 kV the contrast of threading dislocations (TDs) was enhanced. The higher contrast of dislocations was due to the higher ratio of BSE to SE signal at higher beam energies, [28] improving the observation of extended defects over the surface topography. Additionally, beam energy increased the penetration depth of the electron beam, therefore dislocation lines were also visible.

Next, ECCI micrographs at different currents were performed to study its influence on image quality. The objective lens aperture was set to  $30\,\mu m$  to achieve high-resolution observation, restricting the beam current range between 0.2 and 5.7 nA. Figure 4 shows two ECCI micrographs taken at 0.2 nA (Figure 4a) and 5.7 nA (Figure 4b).









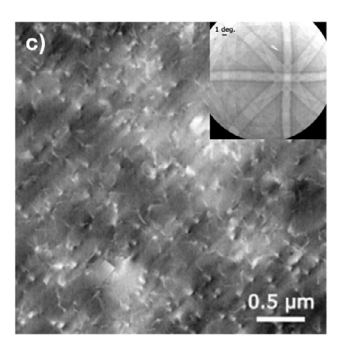


Figure 3. a) SE micrograph of Ga(In)As sample. ECCI micrographs and ECP images in the inset at accelerating voltages of b) 10 kV and c) 30 kV.

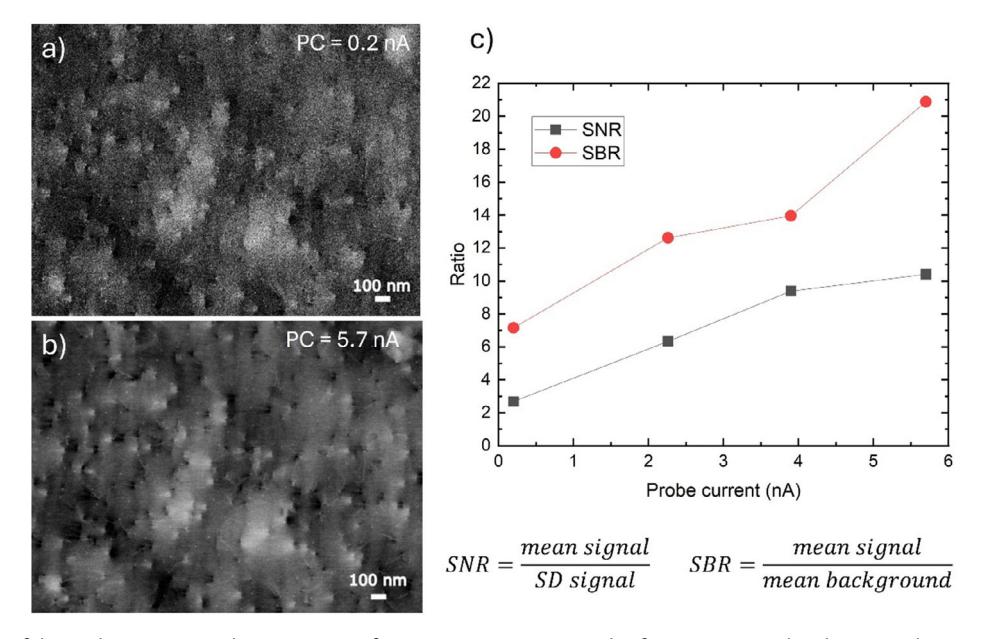


Figure 4. Influence of the probe current on the ECCI image formation. ECCI micrograph of Ga(In)As sample taken at probe current of a) 0.2 nA and b) 5.7 nA. c) SNR and the SBR represented versus the probe current.

The ECCI image quality was quantified by means of evaluating the SNR and the signal-to-background ratio (SBR). Both SNR and SBR were measured on the same sample area for probe currents between 0.2 and 5.7 nA. In Figure 4c the measured SNR and SBR are plotted as a function of the probe current. It can be observed that both ratios (SNR and SBR) increase with increasing probe current.

After analyzing beam energy and current, the beam conditions chosen for the ECCI measurements were the following: beam energy of 30 kV to have a high ratio of BSE to SE signal and beam current of 5.7 nA for high SNR and SBR.

#### 3.2. ECCI at Different Diffraction Conditions

In order to study different diffraction conditions, ECCI measurements of the same sample and the same area were performed. This study was performed with GaSb-on-Si sample.

First, ECP were acquired, then, the sample was aligned at different Kikuchi bands to fulfill different diffraction conditions (g).

ECP of the sample is shown in Figure 5, the observation positions are marked with blue crosses.

Three different cases were studied: First, ECCI measurements were performed with the sample aligned on the same Kikuchi band and opposite band edge, with diffraction conditions  $\mathbf{g}=(2-2\ 0)$  and  $\mathbf{g}=(-2\ 2\ 0)$ , named observation positions P1 and P2, respectively. Second, ECCI measurement were performed with diffraction conditions on the same family of planes with perpendicular orientation,  $\mathbf{g}=(2-2\ 0)$  and  $\mathbf{g}=(-2-2\ 0)$ , named observation positions P1 and P3, respectively. Third, ECCI measurements were performed fulfilling the Bragg condition at different families of planes, in particular,  $\mathbf{g}=(2-2\ 0)$  and  $\mathbf{g}=(-4\ 0\ 0)$ , named observation positions P1 and P4, respectively.

# 3.2.1. Diffraction with $g = (2 - 2 \ 0)$ and $g = (-2 \ 2 \ 0)$

In the first case, the sample was aligned on the same Kikuchi band and opposite band edge, points P1 and P2. In **Figure 6**a,b it is shown with circles the ECCI micrographs for the same TD and



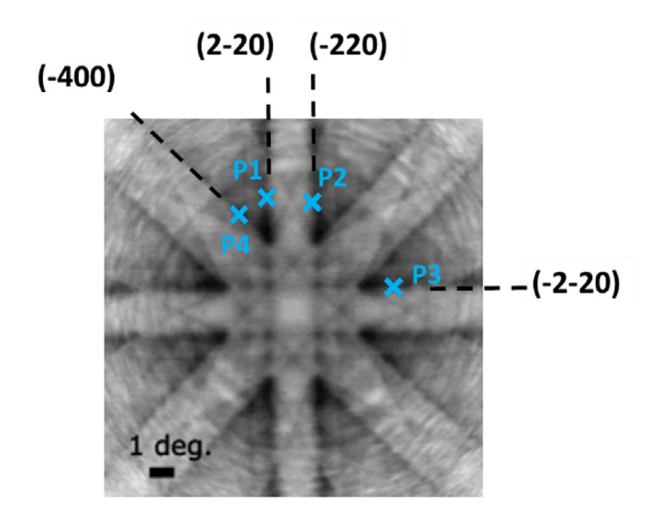


Figure 5. ECP pattern on the GaSb sample under study. Observation positions are marked with blue crosses. Diffraction planes are also indicated.

in Figure 6c,d, with arrows, the same stacking fault (SF). [8,17,29] Micrographs were performed with the sample aligned on the same Kikuchi band and opposite band edge. Figure 6a,c is performed at observation position P1 while Figure 6b,d at P2. The graphs next to each micrograph are the intensity profile over each dislocation/SF.

For P1, the TD showed a bright/dark contrast that was reversed for opposite band edge, P2. For the SFs, the contrast was also reversed for the ECCI micrographs acquired at opposite band edge, showing a bright/dark contrast for P1 that was reversed for P2. Therefore, it was possible to observe that the bright/dark contrast was reversed for each diffraction condition for both types of defects. This contrast inversion at opposite band edge was also observed in interstitial-free steel (Fe–1% Si). [10]

3.2.2. Diffraction with 
$$g = (2 - 2 \ 0)$$
 and  $g = (-2 - 2 \ 0)$ 

On the second case, the crystal lattice planes that fulfill the Bragg condition were perpendicular to each other, named observation positions P1 and P3. In **Figure 7**a,b ECCI micrographs for diffraction condition  $\mathbf{g} = (2 - 2 \ 0)$ , P1, and  $\mathbf{g} = (-2 - 2 \ 0)$ , P3, are shown, respectively.

S. Zaefferer et al.<sup>[29]</sup> applied Bloch wave theory to lattice defect imaging. In the case of a SF, the atoms above and below the defect plane were shifted from each other. Therefore, when the crystal was under diffraction conditions, that is, low BSE intensity, the atoms under the SF were not aligned to the diffraction conditions, that is, high BSE intensity. Assuming the defect plane was inclined, Zaefferer et al. calculated the appearance of an SF on an ECCI micrograph, where there was a bright line corresponding to the intersection of the SF with the surface, the contrast decreased along the side where the SF lies. This is what is observed in the defects marked in Figure 7.

Additionally, it was possible to observe that SFs along the vertical direction (marked with circles) were only observable at diffraction condition  $\mathbf{g}=(2-2\ 0)$ . Also, the intersection of SF along the horizontal direction (marked with arrows) had greater contrast for the perpendicular diffraction condition  $\mathbf{g}=(-2-2\ 0)$ . The effect was caused by the invisibility criteria  $\mathbf{g}\cdot\mathbf{b}=0$  and  $\mathbf{g}\cdot(\mathbf{b}\times\mathbf{u})=0$ . Being  $\mathbf{u}$  the dislocation line. The invisibility criteria are well known in TEM analysis and has been demonstrated to occur in ECCI measurements. However, to observe a clear invisibility, the observation position had to be away from any Kikuchi bands intersection. Therefore, it was possible to have contrast from dislocations that fulfill the invisibility criteria with the diffraction condition under observation.

## 3.2.3. Diffraction with $g = (2 - 2 \ 0)$ and $g = (-4 \ 0 \ 0)$

Third, ECCI measurements were performed fulfilling the Bragg condition at different families of planes, in particular,  $\mathbf{g} = (2-20)$  and  $\mathbf{g} = (-4\ 0\ 0)$ , named observation positions P1 and P4, respectively. ECCI micrographs are shown in **Figure 8**a at P1, b at P4.

Figure 8a shows the ECCI micrograph taken at  $g = (2 - 2 \ 0)$ , in this case, it was possible to observe arrays of point-like defects, marked with circles. Those point-like defects were assumed to

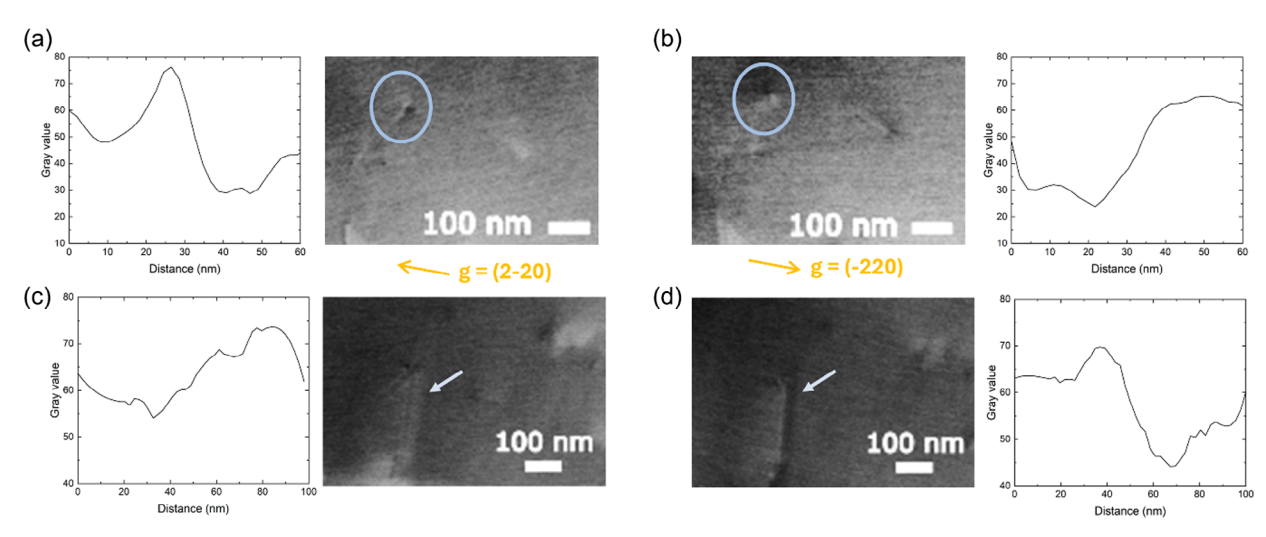


Figure 6. ECCI micrographs of the same defects observed at opposite band edges and the corresponding intensity profiles for the same dislocation a)  $\mathbf{g} = (2 - 2 \ 0)$  and b)  $\mathbf{g} = (-2 \ 2 \ 0)$ , and the same SF c)  $\mathbf{g} = (2 - 2 \ 0)$  and d)  $\mathbf{g} = (-2 \ 2 \ 0)$ .





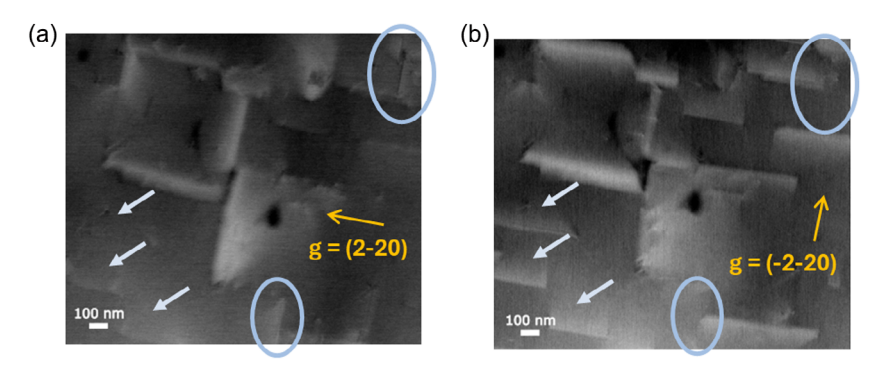


Figure 7. ECCI micrographs observed at perpendicular diffraction condition. a)  $g = (2 - 2 \ 0)$ , P1, and b)  $g = (-2 - 2 \ 0)$ , P3.

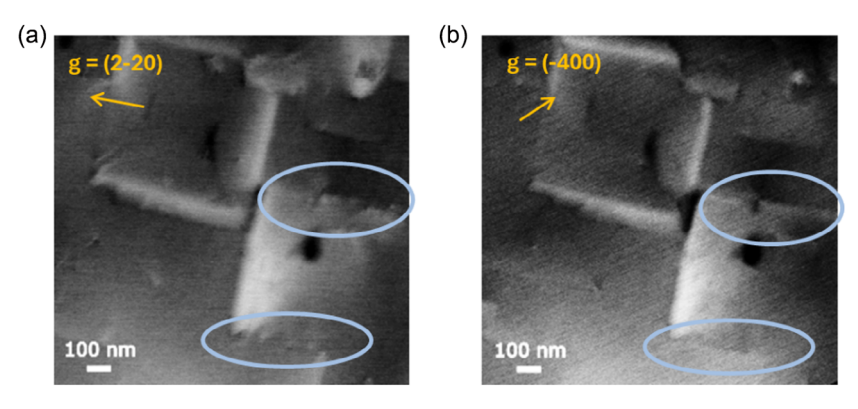


Figure 8. ECCI micrographs observed at different diffraction conditions. a)  $\mathbf{g} = (2 - 2 \ 0)$ , P1, and b)  $\mathbf{g} = (-4 \ 0 \ 0)$ , P4.

be dislocations. However, for  $g = (-4 \ 0 \ 0)$  (Figure 8b) those defects did not appear as point-like defects, in this diffraction condition, they appeared to be line-like defects. This was important because the density of dislocations could vary depending on the diffraction conditions employed for acquiring the ECCI image. To understand this effect, we needed to get into the grounds of the technique and understand how the contrast formation works in ECCI. High-energy electrons interacting with solid matter suffer mainly: i) Bragg scattering (elastic and coherent); ii) phonon scattering (quasielastic and incoherent); iii) core loss scattering (inelastic and incoherent); and iv) multiple loss scattering (inelastic and incoherent). [28,29,31] The backscattering intensity obtained from crystalline materials depends on the crystal lattice parameters and the orientation of the crystal lattice with respect to the primary electron beam direction, where a fraction of the incident electrons undergoes sufficient scattering events and may, eventually, leave the sample through the entry surface. The resulting BSE has a broad energy distribution, but their intensity (i.e., their number) depends on the crystallographic direction/crystal phase parallel to the primary beam. Therefore: 1) The contrast in ECCI images arises from the way the electron beam is scattered by the distorted lattice around the defect. 2) When the electron beam is at a Bragg angle, the scattered electrons create a channeling pattern. 3) Defects like dislocations cause local deviations from this pattern, leading to variations in the intensity of BSE, which are detected and form the image. 4) The visibility of a defect in ECCI depends on the diffraction conditions (the orientation of the crystal relative to the electron beam) and the nature of the defect itself.

Taking this into account, it was possible that the points observed in Figure 8a (g = (2 - 2 0), P1) were dislocations close enough to each other that when moving to  $\mathbf{g} = (-4\ 0\ 0)$ , P4; they could not be resolved and appeared as a continuous line. Another reason behind this effect was that part of the defect fulfilled the invisibility criteria (explained in the previous subsection) and could not be resolved in the same way in both diffraction conditions. It is worth mentioning that this was only a hypothesis and that more experiments must be done to better understand this effect.

## 3.3. Dislocation Density

In regards of defect quantification, the quality of samples is usually given by the defect density, typically, the number of defects per square centimeter. As shown in the previous section, depending on the diffraction condition used for ECCI measurements, defects can have reversed contrast, be invisible or have different appearance. To show this influence, ECCI micrographs were performed at each diffraction condition (P1, P2, P3, and P4 in the previous section) while keeping the same exact area of the sample. For each type of defect and diffraction condition, the defect density was measured, and the standard error of the mean was calculated. In Figure 9, the measured extended defect density of both TD and SF are plotted for each diffraction condition.

First, regarding the extended defect density measured at opposite edges of the same Kikuchi band, the obtained values were





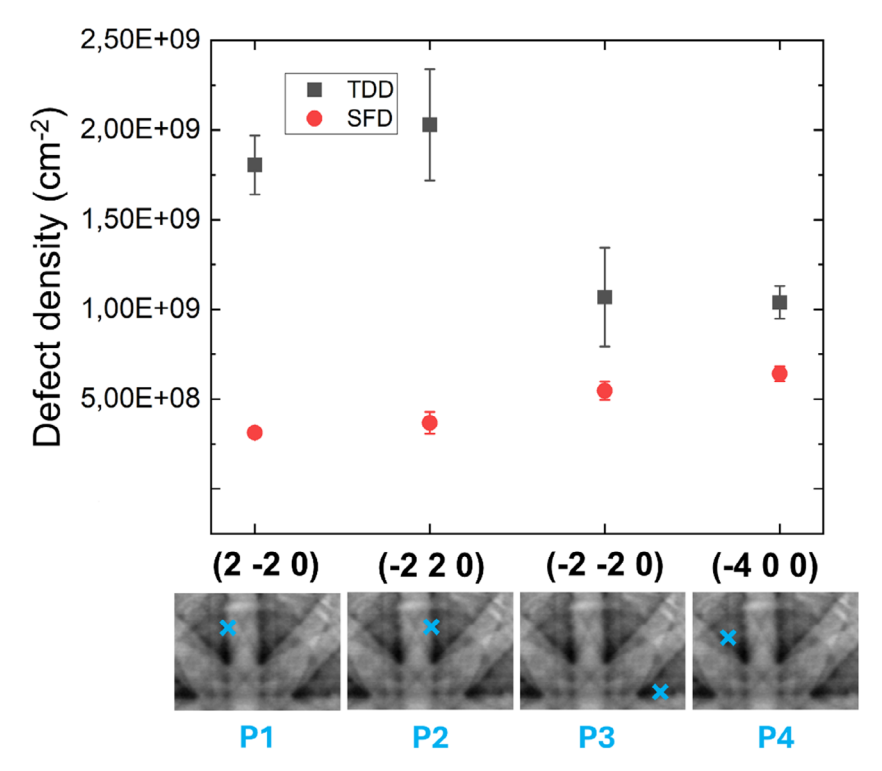


Figure 9. Measured extended defect density as a function of the diffraction condition.

similar. However, when comparing the dislocation density measured at the perpendicular bands, the TD density was 50% lower, while the SF density was 35% higher. Similar results were obtained when comparing extended defect density measured at diffraction conditions with different families of planes. One of the main causes was the invisibility criteria, as explained before, depending on the Burgers vector, the dislocation line, and the diffraction condition, defects might not have been visible. These results showed that ECCI measurements must be performed at more than one diffraction condition, giving a lower limit of extended defect density. Thus, further research and data analysis are needed for obtaining more accurate values. Complementary techniques such as TEM would be helpful for such development. Nevertheless, ECCI has great potential as it enables fast feedback of III-V thin films quality in regards extended defects.

## 4. Conclusion

In this work, we present a comprehensive analysis of the measurement conditions of ECCI for the study of III—V semiconductors. First, the ECCI working principles are explained. Then, electron-beam conditions are studied for measurement optimization. It is found that higher beam energy provides better contrast of dislocation as the ratio of BSE to SE signal is increased. High beam current is also beneficial as it increases both SNR and SBR. Next, different diffraction conditions are explored. ECCI micrographs measured at opposite band edge give opposite contrast of defects and similar density. However, due to the invisibility criteria and how defects are resolved at each diffraction

condition, extended defect density is dissimilar when measured at different bands. Therefore, currently ECCI measurements give a lower value of extended defect density. Nevertheless, in this work the potential of this technique is shown, further development will allow us to achieve accurate values of extended defect density. It is also shown the possibility of studying preferential type of defects, planes or directions as well as the study of individual defects. It is worth mentioning that, in contrast to TEM, ECCI in an SEM is a nondestructive technique that also allows wafer mapping and therefore homogeneity tests that enables scalability and its penetration into industry. In summary, it is demonstrated that ECCI is a very promising technique for fast and cost-effective characterization of defects on III—V semiconductors. Moreover, our study shows how critical the diffraction conditions are for the quantification of the dislocation density.

# Acknowledgements

This work was supported in part by the project "Zero-loss Energy harvesting Using nanowire solar cells in Space", funded by the European Union, Horizon Europe, EIC Project 101161465 (ZEUS). M.S.L. acknowledges financial support from the Generalitat Valenciana (Project: CIAPOS/2021/293). L.M.B. acknowledges Ayuda a Primeros Proyectos de Investigación (PAID-06-24), Vicerrectorado de Investigación de la Universitat Politècnica de València (UPV). V.J.G. acknowledges the Generalitat Valenciana (CDEIGENT/2020/009, and ESGENT/2024/17), the Conselleria de Educación, Universidades y Empleo under the NIRVANA Grant (PROMETEO Program, CIPROM/2022/14), and to the AGENCIA ESTATAL DE INVESTIGACIÓN of Ministerio de Ciencia, Innovacion y Universidades Grant CNS2023-145093 funded by MICIU/AEI/10.13039/501100011033 and by "European Union NextGenerationEU/PRTR". All authors acknowledge AGENCIA ESTATAL DE INVESTIGACIÓN of



www.advancedsciencenews.com



Ministerio de Ciencia e Innovacion (PID2024-162261NB-I00 and EQC2021-007244-P) and to the European Regional Development Fund (ERDF) (IDIFEDER/2020/041, IDIFEDER/2021/061), and the Quantum Communications program supported by Ministerio de Ciencia e Innovacion (MCIN) with funding from European Union NextGenerationEU (PRTR-C17.I1) and by Generalitat Valenciana (COMCUANTICA/003).

## Conflict of Interest

The authors declare no conflict of interest.

# **Data Availability Statement**

The data that support the findings of this study are available from the corresponding author upon reasonable request.

## **Keywords**

characterization, dislocations, electron channeling contrast imaging, III–V semiconductors

Received: July 15, 2025 Revised: September 29, 2025 Published online:

- [1] P. Dong, Y.-K. Chen, G.-H. Duan, D. T. Neilson, *Nanophotonics* **2014**, 3, 215.
- [2] A. Y. Liu, J. Bowers, IEEE J. Sel. Top. Quantum Electron. 2018, 24, 1.
- [3] E. Tournié, L. M. Bartolome, M. R. Calvo, Z. Loghmari, D. A. Díaz-Thomas, R. Teissier, A. N. Baranov, L. Cerutti, J.-B. Rodriguez, *Light Sci. Appl.* 2022, 11, 165.
- [4] P. Mouriño, L. Mercadé, M. S. Lozano, R. Resta, A. Griol, K. B. Saddik, E. Barrigón, S. Fernández-Garrido, B. J. García, A. Martínez, V. J. Gómez, Adv. Mater. Technol. 2024, 9, 2400525.
- [5] Q. Li, K. M. Lau, Prog. Cryst. Growth Charact. Mater. 2017, 63, 105.
- [6] L. Reimer, H. Kohl, Transmission Electron Microscopy: Physics of Image Formation, Springer, New York, NY 2008.
- [7] D. C. Joy, D. E. Newbury, D. L. Davidson, J. Appl. Phys. 1982, 53, R81.
- [8] S. D. Carnevale, J. I. Deitz, J. A. Carlin, Y. N. Picard, D. W. McComb, M. D. Graef, S. A. Ringel, T. J. Grassman, IEEE J. Photovolt. 2015, 5, 676.

- [9] P. Morin, M. Pitaval, E. Vicario, G. Fontaine, Scanning 1979, 2, 217.
- [10] H. Kriaa, A. Guitton, N. Maloufi, Sci. Rep. 2017, 7, 9742.
- [11] M. Feifel, J. Ohlmann, R. M. France, D. Lackner, F. Dimroth, J. Cryst. Growth 2020, 532, 125422.
- [12] A. Blumer, M. Baan, Z. Blumer, J. Boyer, T. J. Grassman, *Microsc. Microanal.* 2021, 27, 912.
- [13] S. Fan, R. Liu, Y. Huang, J. Liu, X. Zhan, X. Sun, M. Feng, Y. Yin, Q. Sun, H. Yang, J. Appl. Phys. 2022, 132, 105302.
- [14] C. Shang, J. Selvidge, E. Hughes, J. C. Norman, A. A. Taylor, A. C. Gossard, K. Mukherjee, J. E. Bowers, *Phys. Status Solidi A* 2021, 218, 2000402.
- [15] J. S. Mangum, S. Theingi, A. N. Neumann, W. E. McMahon, E. L. Warren, J. Cryst. Growth 2022, 581, 126490.
- [16] D. Jung, P. G. Callahan, B. Shin, K. Mukherjee, A. C. Gossard, J. E. Bowers, J. Appl. Phys. 2017, 122, 225703.
- [17] P.-C. (Brent) Hsu, H. Han, E. Simoen, C. Merckling, G. Eneman, Y. Mols, N. Collaert, M. Heyns, *Phys. Status Solidi A* 2019, 216, 1900293.
- [18] S. D. Carnevale, J. I. Deitz, J. A. Carlin, Y. N. Picard, M. De Graef, S. A. Ringel, Appl. Phys. Lett. 2014, 104, 2321111.
- [19] A. Gilbert, K. Graser, M. Ramonda, A. Trampert, J.-B. Rodriguez, E. Tournié, Adv. Phys. Res. 2025, 4, 2400126.
- [20] M. E. Twigg, Y. N. Picard, J. D. Caldwell, C. R. Eddy JR., M. A. Mastro, R. T. Holm, P. G. Neudeck, A. J. Trunek, J. A. Powell, J. Electron. Mater. 2010, 39, 743.
- [21] H. Han, T. Hantschel, L. Strakos, T. Vystavel, M. Baryshnikova, Y. Mols, B. Kunert, R. Langer, W. Vandervorst, M. Caymax, Ultramicroscopy 2020, 210, 112928.
- [22] A. Schulze, L. Strakos, T. Vystavel, R. Loo, A. Pacco, N. Collaert, W. Vandervorst, M. Caymax, *Nanoscale* 2018, 10, 7058.
- [23] S. Nishikawa, S. Kikuchi, Nature 1928, 122, 726.
- [24] C. G. Van Essen, E. M. Schulson, J. Mater. Sci. 1969, 4, 336.
- [25] KOSSEL and KIKUCHI Simulation (K-Patterns) [Online], http://jcrystal.com/products/kossel/index.htm (accessed: July 2025).
- [26] A. J. Wilkinson, G. R. Anstis, J. T. Czernuszka, N. J. Long, P. B. Hirsch, Philos. Mag. A 1993, 68, 59.
- [27] A. J. Wilkinson, Philos. Mag. Lett. 1996, 73, 337.
- [28] J. I. Goldstein, D. E. Newbury, J. R. Michael, N. W. M. Ritchie, J. H. J. Scott, D. C. Joy, Scanning Electron Microscopy And X-ray Microanalysis, Springer, New York, NY 2018.
- [29] S. Zaefferer, N.-N. Elhami, Acta Mater. 2014, 75, 20.
- [30] M. A. Crimp, B. A. Simkin, B. C. Ng, Philos. Mag. Lett. 2001, 81, 833.
- [31] W. Sigle, Annu. Rev. Mater. Res. 2005, 35, 239.